PNAS
www.pnas.org

Supplementary Information for

Large Enhancement of Thermoelectric Performance in MoS_2/*h*-BN Heterostructure due to Vacancy-induced Band Hybridization

Jing Wu[a,b,1], Yanpeng Liu[b,c,d,1], Yi Liu[b,e], Yongqing Cai[f], Yunshan Zhao[b,e,g], Hong Kuan Ng[a,h], Kenji Watanabe[i], Takashi Taniguchi[i], Gang Zhang[j], Cheng-Wei Qiu[b,e,k], Dongzhi Chi[a], AH Castro Neto[b,h], John TL Thong [b,e,2], Kian Ping Loh [b,c,k,2], Kedar Hippalgaonkar [a,b,l,2]

[a]Institute of Materials research and Engineering , Agency for Science, Technology and Research, 138634, Singapore; [b]Centre for Advanced 2D Materials, National University of Singapore, 117546, [c]Department of Chemistry, National University of Singapore, 117542, Singapore; [d]Key Laboratory for Intelligent Nano Materials and Devices of Ministry of Education, and Institute of Nanoscience, Nanjing University of Aeronautics and Astronautics, Nanjing 210016, China; [e]Department of Electrical and Computer Engineering, National University of Singapore, 117583, Singapore; [f]Joint Key Laboratory of the Ministry of Education, Institute of Applied Physics and Materials Engineering, University of Macau, Taipa, Macau, China; [g]School of Physics and Technology, Nanjing Normal University, Nanjing 210023, China; [h]Department of Physics, National University of Singapore, 117542; [i]Advanced Materials Laboratory, National Institute for Materials Science, 1-1 Namiki, Tsukuba 305-0044, Japan; [j]Institute of High Performance Computing, Agency for Science, Technology and Research, 138632, Singapore; [k]Shenzhen University-National University of Singapore Collaborative Innovation Center for Optoelectronic Science and Technology, Shenzhen University, Shenzhen, 518060, China; [l]Department of Materials Science and Engineering, Nanyang Technological University, 50 Nanyang Avenue, 639798, Singapore;

[2]To whom correspondence should be addressed. Email: kedar@ntu.edu.sg (K.H.); chmlohkp@nus.edu.sg (K.P. L.) or elettl@nus.edu.sg (J.T.L.T.); [1]These authors contributed equally to this work.

www.pnas.org/cgi/doi/10.1073/pnas.2007495117

Table of Contents

S1. **Sample fabrication:**

MoS_2 and *h*-BN flakes were separately mechanically exfoliated onto SiO_2/Si substrates, then examined by optical microscope (optical contrast in both bright-field and dark-field mode) and AFM to ensure that the surface, geometry and thickness are suitable for subsequent measurements (Fig. S1 a-d). Clean MoS_2 flakes with well-defined shape and uniform thickness were then spincoated with poly(methyl methacrylate) (PMMA) followed by baking in air 180 °C for 2 minutes . Next, the sample (with PMMA) is rinsed in 30 *w.t.*% KOH solution at room temperature. Once the PMMA film detaches from the substrate, the PMMA film with MoS_2 flake is fished out and rinsed in deionized (DI) water several times to remove any KOH residue. The MoS2-on-*h*BN heterostructure is fabricated by transferring the MoS_2 flake onto pre-identified *h*-BN flakes using standard transfer techniques[S1]. Once stacked, the heterostructure is baked at ~100℃ for 20 minutes, then cooled down to room temperature. The heterostructure is soaked in acetone for 2 hours to remove the PMMA film. After which, electrodes were patterned by standard EBL process, followed by deposition of titanium/gold (Ti/Au) of thickness of 3 nm and 70 nm respectively. Ti was chosen owing to its low work function to match the electron affinity of MoS_2 to form ohmic contacts. Fig. S1 shows the typical routine for device fabrication. For comparison, MoS_2/SiO_2 sample with the same flake thickness, channel dimension and electrode components were also fabricated (Fig. S1 f).

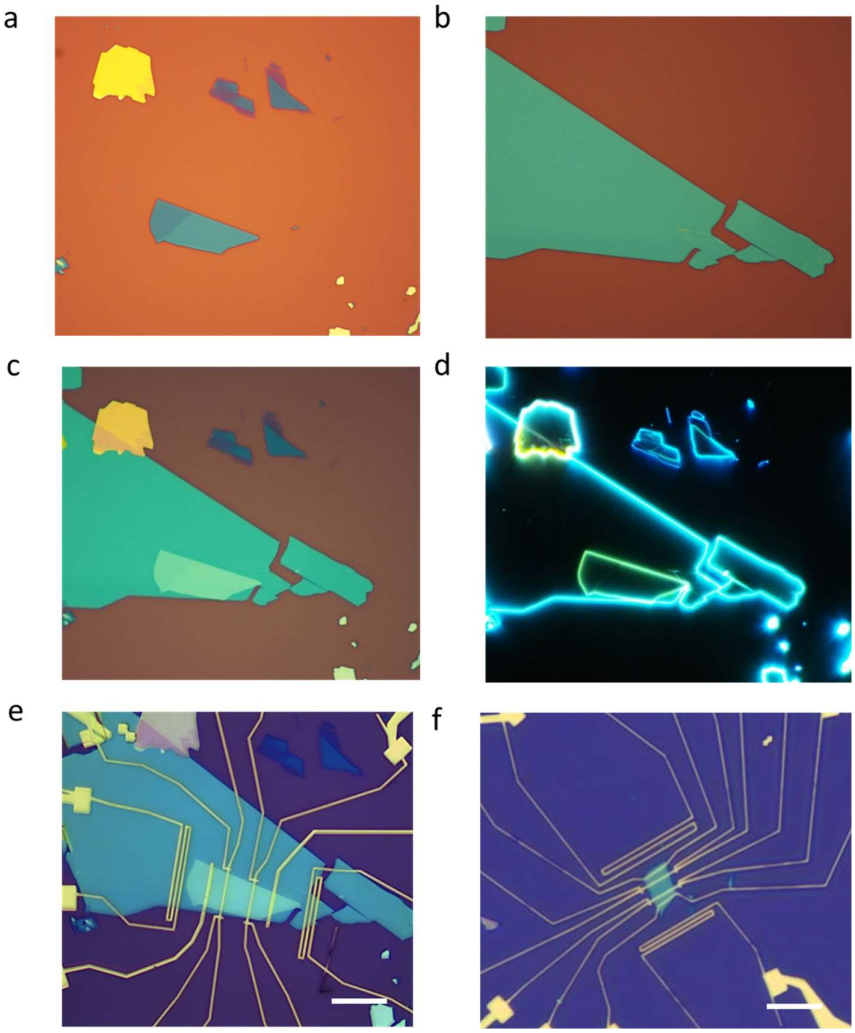

Figure S1: Detailed steps of sample fabrication (a-e). a and b, Mechanical exfoliated MoS_2 and *h*-BN on SiO_2/Si substrate. **c and d,** Bright- and Dark-field image of stacked heterostructure respectively. **e** and **f**, Optical images of MoS_2/*h*-BN and MoS_2/SiO_2 devices (scale bar is 10 μm).

The thicknesses of MoS_2 and *h*-BN flakes were determined using a Dimension FastScan Bruker AFM (Fig. S2). The average thickness of monolayer MoS_2 is around 0.65 nm. This indicates that our MoS_2 flake is six layers thick, also confirmed by the optical contrast method[S2] and STS measurement. The thickness of *h*-BN substrate is around 30 nm.

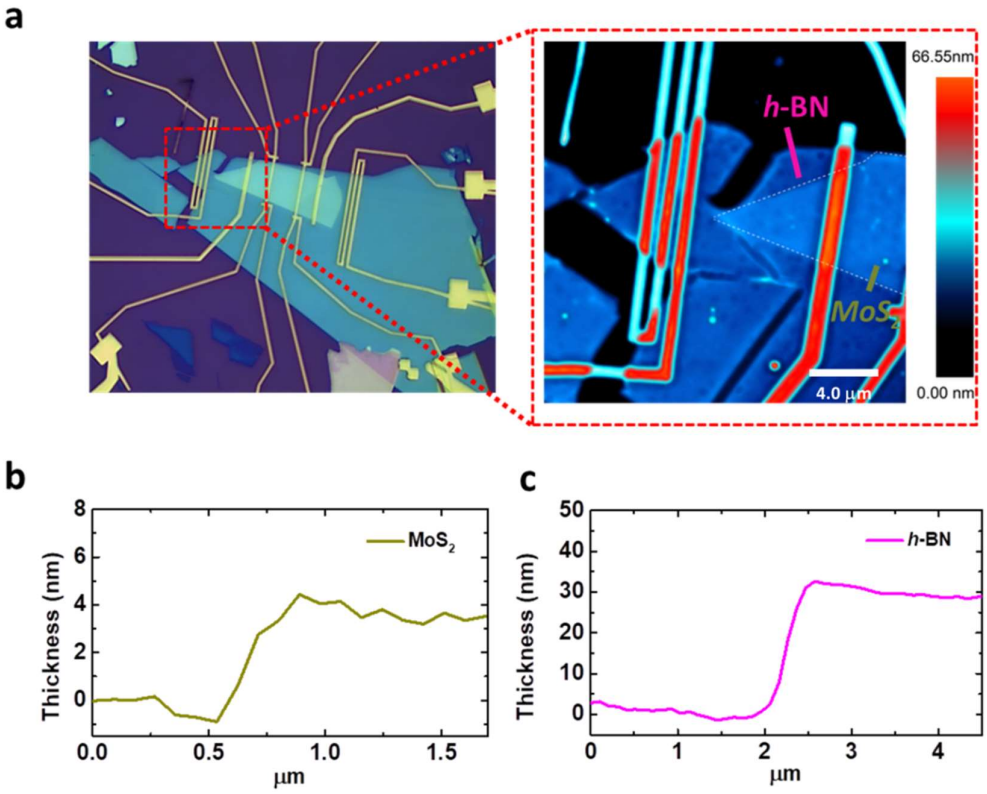

Figure S2: AFM characterization of MoS_2/*h*-BN device. a, Optical (left) and AFM (right) images of a typical FET device. **b**, Line profiles of MoS_2 and *h*-BN flake used in this study.

S2. STM and STS measurement

The STM and STS measurements were performed using Omicron ultrahigh-vacuum LT-STM (< 10^{-10} torr). Before measurement, the tungsten tip was calibrated by Au (111) crystal. During measurements, the sample is grounded through the deposited Ti/Au electrode on top of the MoS_2 flake. The gate electrode is lead out by an aluminum wire. After wire-bonding, the MoS_2/*h*-BN sample was annealed at 220 ºC in the preparation chamber (<10^{-10} torr) to remove absorbents and to form better contacts. STM and STS data were collected at liquid Helium temperatures. Constant-current mode was employed to capture STM images and external lock-in technique was employed to record STS data.

S3. Lattice constant of MoS_2 crystal from STM

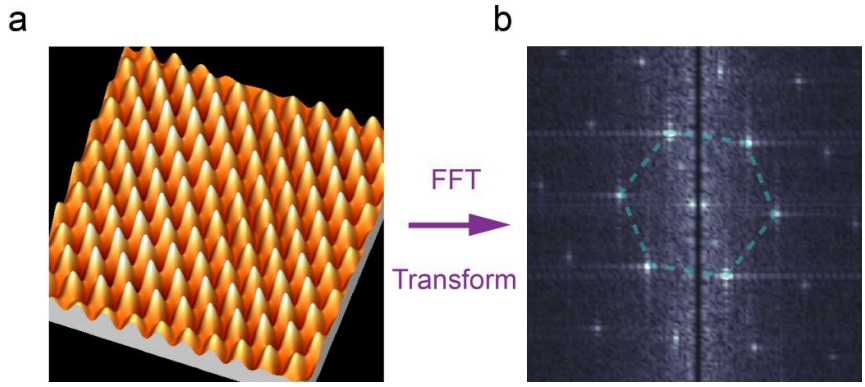

Figure S3: 3D STM image of MoS_2 (a) and its corresponding fast Fourier transform (FFT) image (b) showing the pattern of sulfur lattices.

S4. **First-principles computational details**

First-principles calculations based on spin-polarized density functional theory with consideration of spin-orbit coupling effect are conducted using the Vienna Ab initio simulation package (VASP).[S3] The weak *van der Waals* (vdW) interactions in multilayer MoS_2 are calculated with the Becke88 optimization (optB88) function. A kinetic energy cutoff of 400 eV and a 3×3×1 (single Γ) Monkhorst−Pack grid is adopted for MoS_2 unit cell (7×7 supercell). All the atomic models are created by inserting a vacuum slab with a thickness of 15 Å to avoid possible spurious interactions between image layers. All structures are fully relaxed until the force on each atom is smaller than 0.01 eV/Å.

S5. **X-ray photoelectron spectroscopy (XPS) of MoS_2/*h*-BN heterostructure:**

XPS result confirms no other magnetic or alternate crystal impurities that could have been formed during either crystal growth or surface absorbents during flake transfer. The core level spectrums of Mo $3d_{5/2}$, $3d_{3/2}$ and S $2p_{3/2}$ $2p_{1/2}$ are shown in Fig. S4 a and b, respectively. The Mo $3d_{5/2}$, $3d_{3/2}$ and S $2p_{3/2}$ $2p_{1/2}$ spectrum are well-fitted using Lorentzian and Gaussian combination functions and their centers are located at 230.2 eV, 233.4 eV, 163.0eV and 164.2eV, suggesting the high elemental purity of MoS_2 and a slight n-doping in as-exfoliated flakes. Moreover, a wide scan over the whole MoS_2 flake shows no other additional elemental peaks (Fig. S4 c), confirming that the sub-band spin splitting observed in defective MoS_2 is indeed due to sulfur vacancies.

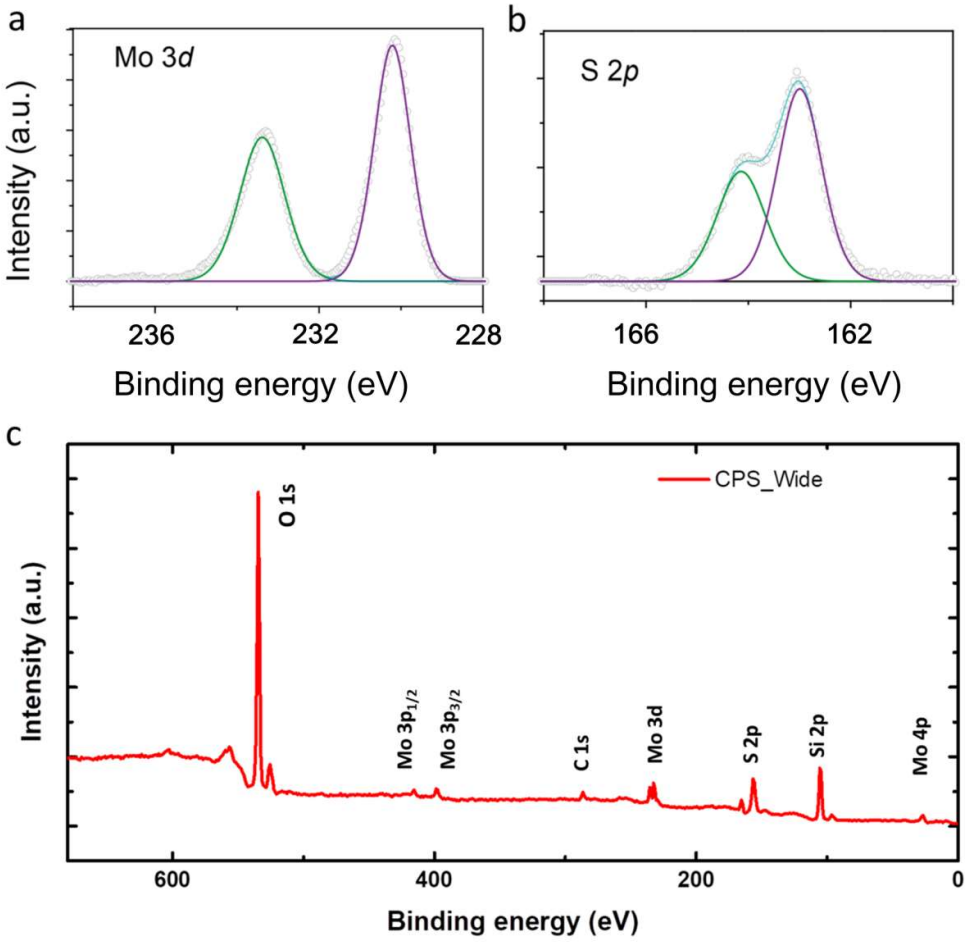

Figure S4: a and **b**, High resolution x-ray photoemission spectroscopy (XPS) scan of Mo 3*d* and S 2*p* for MoS_2. **c**, Wide scan XPS of our sample.

S6. **Calculations of electrical conductivity and mobility**

4-probe measurements were employed to eliminate contact resistance and to extract a precise electrical conductivity for MoS_2 flakes at different gate voltages (Fig. S5). The linear *I-V* curves indicate ohmic contact between the metal electrodes and the flake. Each data point in the gate-dependent transfer curve contains an *I-V* curve where its slope can be extracted as shown in Fig. S6.

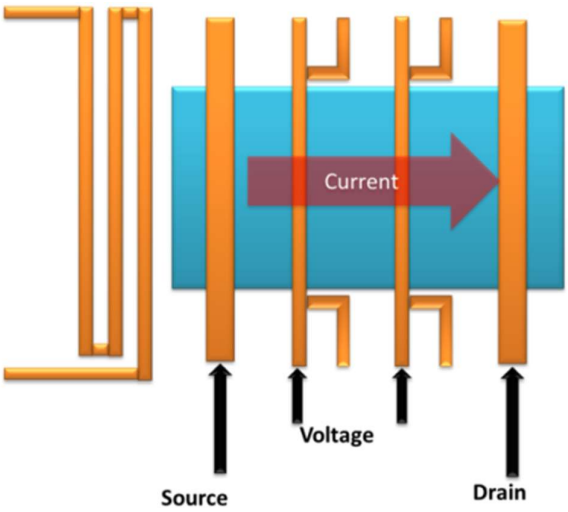

Figure S5: Illustration of 4-probe electrical characterization.

The temperature-dependent mobility is extracted from transfer characteristics (Fig. S6), *via* $\mu_{FE} = \frac{1}{C_{ox}} \frac{d\sigma}{dV_g}$, where $C_{ox} = 12 \times 10^{-9}$ F/cm^2 is the capacitance for 285nm-thick SiO_2. Electrical conductivity ($\sigma = \frac{L}{Wd} G$) can be calculated from G by considering its geometry.

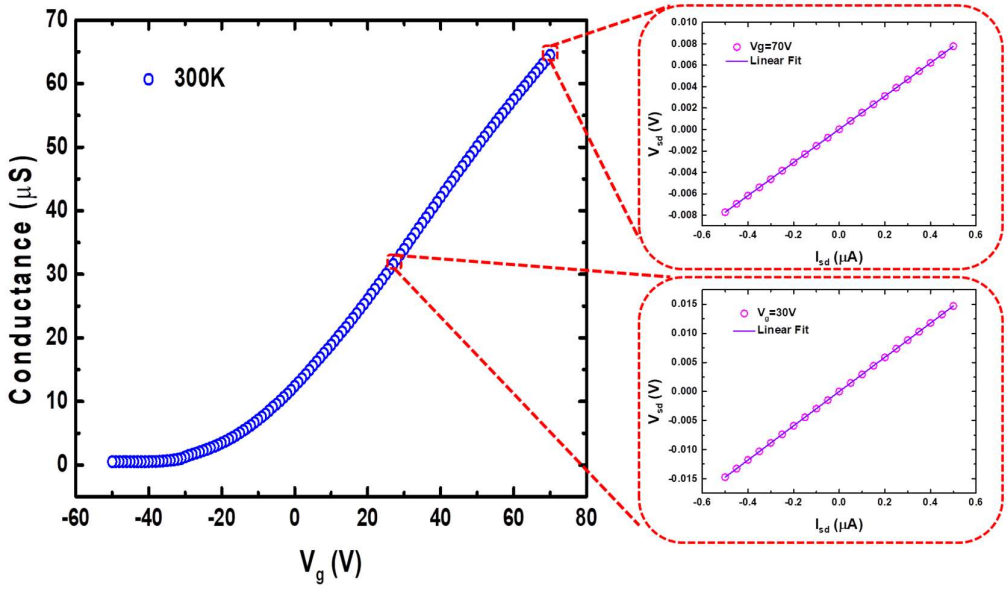

Figure S6: Gate dependent 4-probe conductance of MoS_2 on *h*-BN substrate.

Furthermore, the contact resistance of a representative sample at different temperatures can be ascertained through the difference between 2-probe and 4-probe resistances (Fig. S7). The contact resistance is found to be around 5-10 kΩ in the metallic regime (above 30V gate voltage), which is comparable with previous reports [S4] and is sufficient to provide good electrical contacts with our MoS_2 channel.

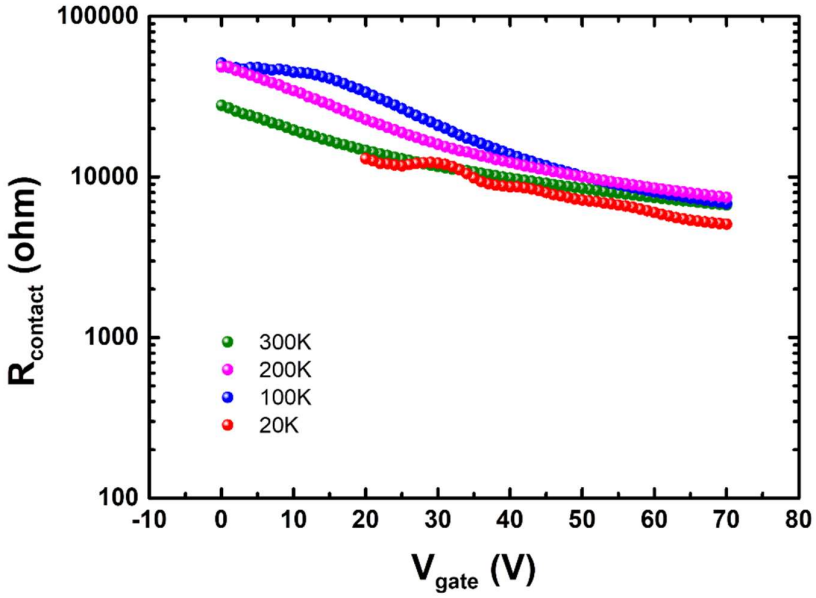

Figure S7: The contact resistance extracted from the difference between 2-probe and 4-probe IV curves as a function of the gate voltage at different temperatures.

Moreover, all of our samples did not show any hysteresis during electrical performance measurement after annealing under high vacuum. Fig. S8 shows 2-probe FET measurements as an example at different temperatures, where the I_d-V_g curves contain no hysteresis during the gate voltage sweep.

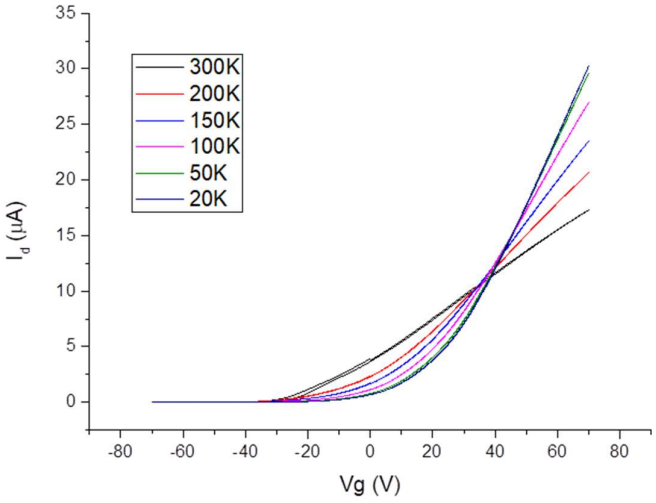

Figure S8: 2-probe FET measurements for MoS_2/*h*-BN sample for different temperatures.

S7. **Seebeck coefficient measurement:**

The Seebeck coefficient $S = V_{TEP}/\Delta T$ of a material is defined as the temperature difference (ΔT) induced open-circuit voltage (V_{TEP}). The measurement of Seebeck coefficient is thus divided into two parts: the measurement for V_{TEP} and ΔT. To measure the Seebeck coefficient, a temperature gradient is realized by applying a DC current bias (I) through a micro-fabricated metal heater using a source-meter (Keithley 6221), thereby generating Joule heating and thus a temperature gradient along the sample. This temperature gradient then generates a thermoelectric voltage V_{TEP}, which is measured by a voltmeter (Keithley 6430).

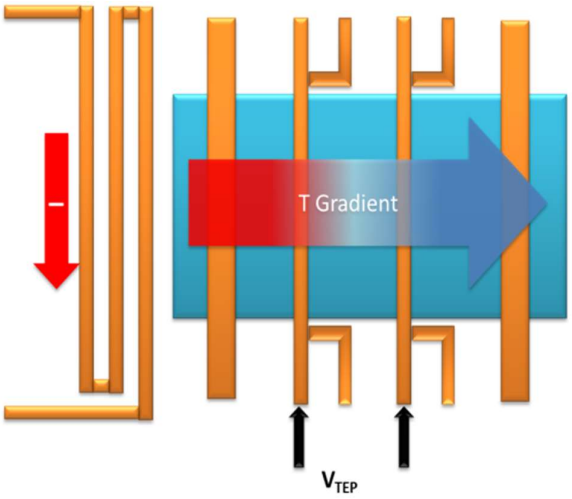

Fig. S9: Schematic of thermoelectric characterization.

The schematic for V_{TEP} measurements is illustrated in Fig. S9. By applying a DC current bias to the heater with increasing values, the corresponding V_{TEP} were recorded. At each current step, the current was held for at least 30 seconds for temperature stabilization prior to measuring V_{TEP}. Due to the relationship of $V_{\mathrm{TEP}} \propto \Delta T \propto I^2R$, the recorded

V_{TEP} exhibits a parabolic behavior following I^2. Typical $V_{TEP} \sim I$ curves are shown in Fig. S10, where concave up/down-ward parabolic curves indicate positive/negative V_{TEP}. Such a clean parabolic V_{TEP} signal indicates that the measured voltage is arising from the thermoelectric transport rather than other sources. It should be noted that as the back-gate is gradually reduced, the transport behavior of MoS_2 shifts from metallic to semiconductor and eventually to insulator. Once the resistance of MoS_2 increases to the range of the input impedance of our voltmeter, the parabolic behavior of V_{TEP} signal disappears and the error bar increases tremendously. Therefore, only data with well-defined parabolic V_{TEP} behavior is extracted to increase the accuracy of our V_{TEP} measurement.

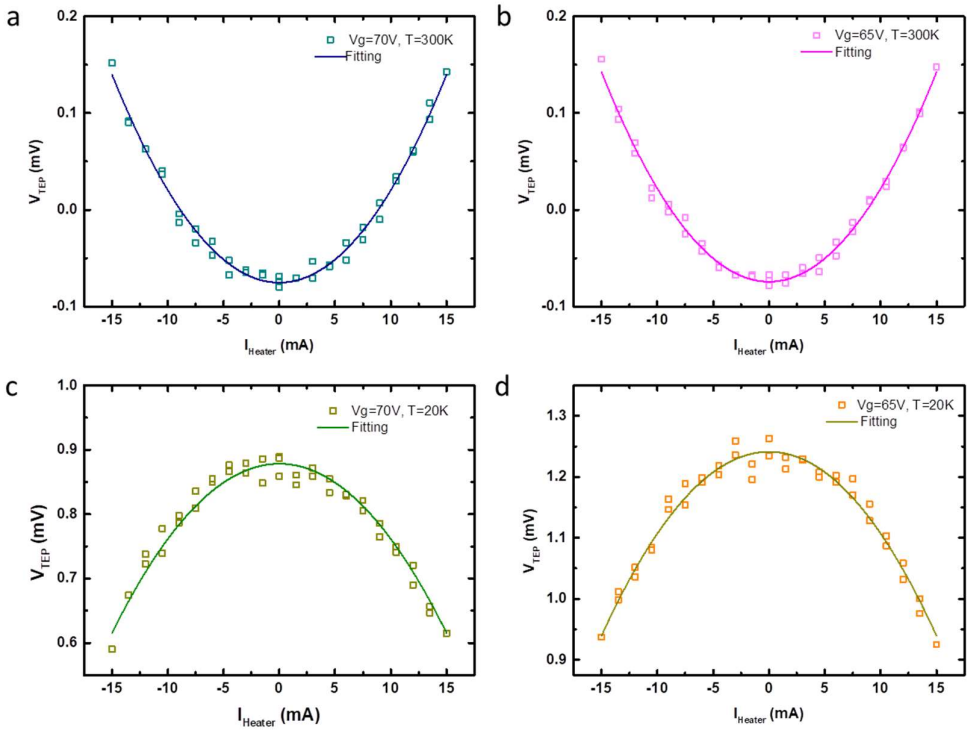

Figure S10: Open-circuit voltage *vs.* heating current. The parabolic fittings R-square is around 0.96~0.99.

To obtain the Seebeck coefficient, the temperature difference ΔT corresponding to V_{TEP} is necessary.

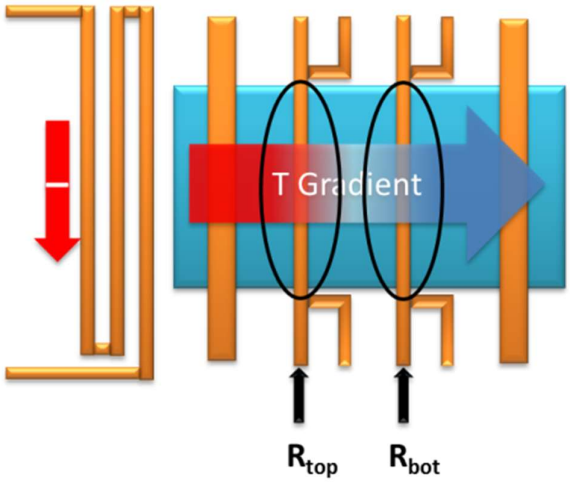

Figure S11: Schematic drawing of experimental setup to capture temperature gradient.

The measurement of ΔT is based on the four-probe resistance (R) of the metal lines (circled in black) used to probe V_{TEP}, as R is sensitive to local temperature (Fig. S11). This measurement is composed of two steps. Step 1: The heater is off without introducing any current. The temperature of the entire sample was controlled globally by a temperature controller (Lakeshore 335), and the resistance R of each sensor was recorded as a function of temperature. The four-probe R were measured by lock-in amplifiers (SR830), where a tiny AC current (~3μA) is fed to measure the induced voltage at a given frequency (13.373 Hz). A typical temperature-coefficient of resistance calibration curve is shown in Fig. S12a, which can be well described by a 5th order polynomial function (slope extracted from the 5th order polynomial fitting produced similar results as the local linear fitting). Step 2: A series of current bias is applied to the heater, same as those used during the V_{TEP} measurement process. Simultaneously, the corresponding R were recorded at each I step. A typical R - I curve

is shown in Fig. S12 c&d, which is also parabolic due to the relation of $R \propto \Delta T \propto I^2R$. Based on the calibration in Step 1, the local temperature of each sensor can be obtained, so that ΔT can be obtained as well. A typical ΔT as a function of temperature is shown in Fig. S12 b. Based on the measured negative V_{TEP} and ΔT, the Seebeck coefficient can be obtained as $S = V_{TEP}/\Delta T$.

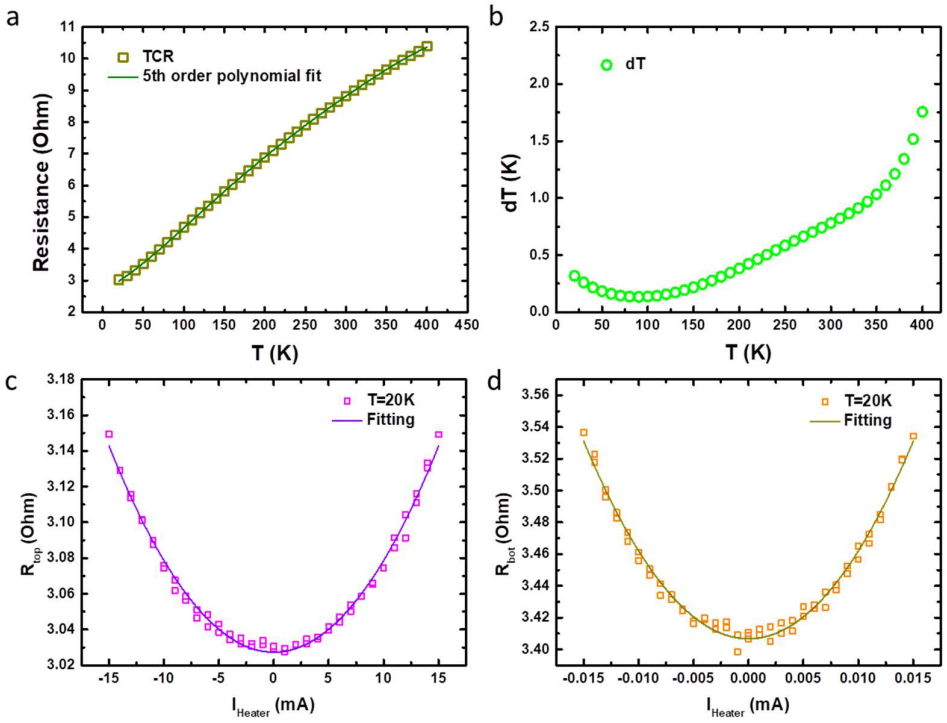

Figure S12: Temperature calibration and characterization of thermoelectric measurements.

S8. **Bandgap determination for MoS_2 flakes:**

Based on the statistical analysis of STS curves, the electronic bandgap (E_g) of six-layer MoS_2 sample was determined to be 1.4 eV, which is comparable with our DFT calculated indirect band-gap band structure as shown in Fig. 1b. We follow a standard procedure to determine the VBM, CBM and E_g.[S5] We first convert our STS curves into logarithmic scale (Fig. S13). Mean value of the signal with the gap was plotted in red horizontal line ($C_{g,av}$). Using linear fittings of the CB and VB band near the edge, the E_{VBM} and E_{CBM} are determined at the intersection of the lines as illustrated in Fig. S13 below. Therefore, the electronic bandgap can be calculated using the equation: $E_g = E_{CBM} - E_{VBM}$.

Our STS data also reveals that the MoS_2 flakes are heavily n-doped, which is confirmed from the position of the Fermi energy (E_F) to the conduction band minimum (CBM) energy.

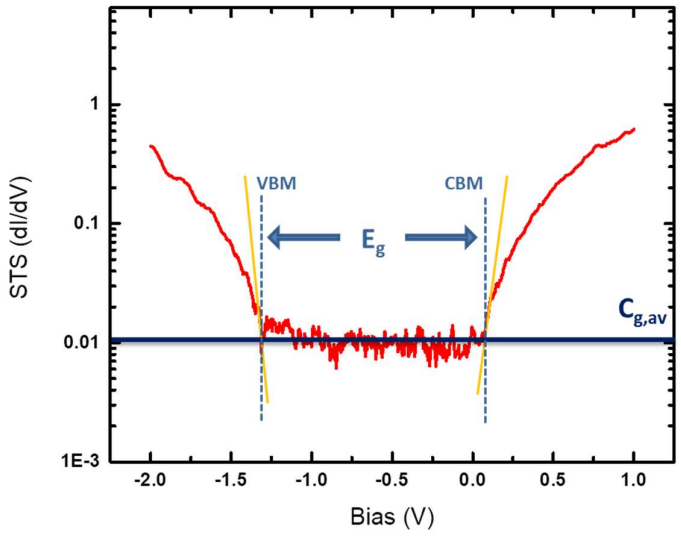

Figure S13: bandgap of 6-layer MoS_2 determined from STS spectra.

S9. Controlling concentration of sulfur vacancies in MoS_2 *via* thermal annealing

To estimate defect density, multiples areas are randomly captured from a few MoS_2 flakes (exfoliated from the same MoS_2 source crystal) and calculated the average defect density from the STM images. Typical STM image scans are shown in Fig. S14.

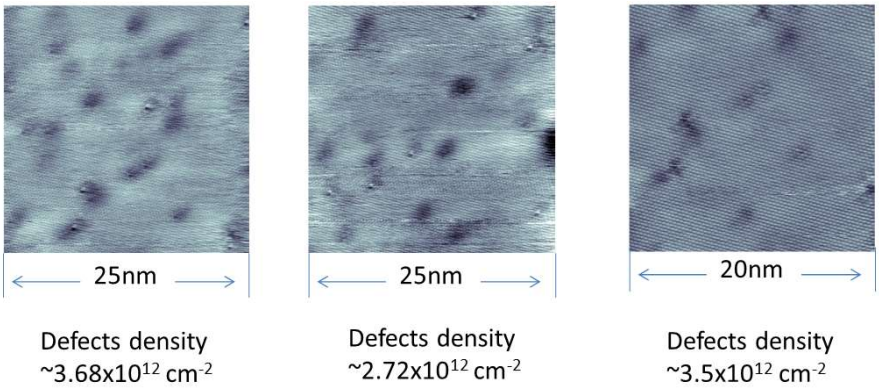

Figure S14: STM of defected MoS2 from various areas and flakes.

Thermal annealing in UHV chamber is found to be capable of creating additional sulfur vacancies in MoS_2 (Fig. S15). The desired density of vacancies could be realized by the precise selection of annealing temperature.

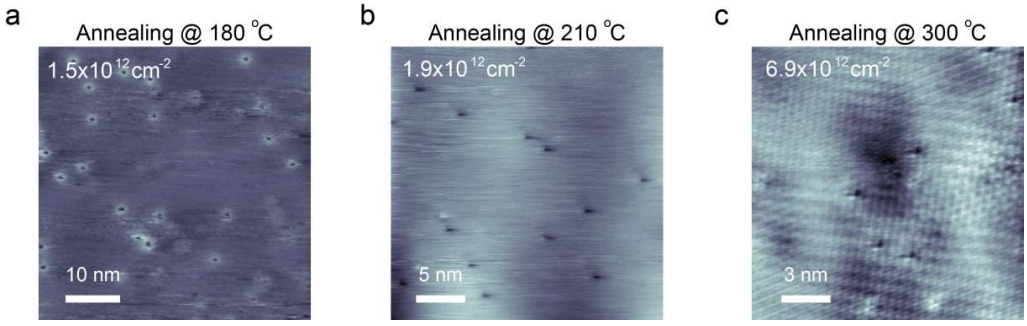

Figure S15: STM topographic images of defective MoS_2 crystal at various annealing processes. The density of sulfur vacancies of the top-layer MoS_2 are verified to be 1.5×10^{12} cm^{-2}, 1.9×10^{12} cm^{-2}, 6.9×10^{12} cm^{-2} after annealing at 180°C, 210 °C and 300 °C for 10 hours, respectively.

For a fixed temperature, it is found that after annealing for a long period of time (around

4 hours), the samples reach a stable state and the increase in defect density also saturates unless the annealing temperature is further increased. This is also corroborated by electric measurements shown in Fig. S16

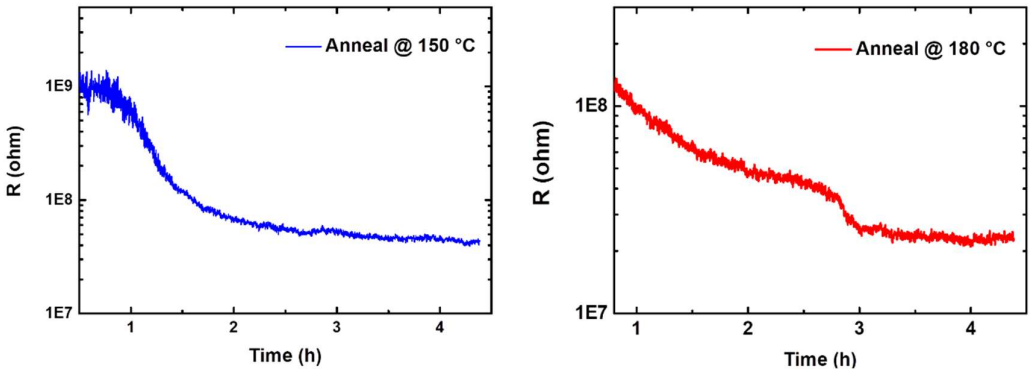

Figure S16: Monitoring the resistance as function of time for different annealing temperatures.

From the curves, for a fixed annealing temperature, the resistance is found to decrease in the beginning due to the n-doping by sulfur vacancies [S6]. After 3 hours, the resistance attains steady-state as the defect level saturates. When the annealing temperature is increased, the resistance starts to decrease again until it saturates at lower values of resistance, as expected.

S10. **Temperature dependent mobility of MoS_2/*h*-BN and MoS_2/SiO_2 device:**

In a dilute gas, in the single particle transport picture under the relaxation time approximation, mobility μ is the result of multiple scattering mechanisms, and can be estimated *via* Mathiessen's rule as $\mu^{-1} = \mu_{\mathrm{imp}}^{-1} + \mu_{\mathrm{ph}}^{-1}$, where μ_{imp} is the impurity-limited mobility and μ_{ph} is the phonon-limited mobility. For MoS_2 at high temperatures, μ is mainly limited by optical phonon (OP) scattering, following a power law of $\mu \sim T^{-\gamma}$ for temperatures higher than $\sim 100\mathrm{K}$. [S7] In our MoS_2/*h*-BN device, we obtained $\gamma \sim 2.1$, in line with theoretically predicted expectations of optical phonon limited mobility μ_{OP} with an exponent of $\gamma \sim 1.7$ [S8] for monolayer and $\gamma \sim 2.6$ [S9] for bulk MoS_2 indicating the high quality of our flakes.(Fig. 3c) In addition, the room temperature mobility, μ_{FE} of $\sim 51\ \mathrm{cm^2V^{-1}s^{-1}}$ is amongst the higher values reported in literature. [S6, S10] At low temperatures (60K), μ_{FE} is ~405 $\mathrm{cm^2V^{-1}s^{-1}}$, which is much higher than the MoS_2/SiO_2 device (~200 $\mathrm{cm^2V^{-1}s^{-1}}$). In this low temperature region, for MoS_2/SiO_2 device, there is a deviation from the simple power law $\mu \sim T^{-\gamma}$ and a saturation or slight decrease of μ is observed, resulting in $d\mu/dT \sim 0$ as $T \rightarrow 0$. However, in MoS_2/*h*-BN device, the conduction electrons are coupled strongly with the localized vacancy states, which result in band hybridization at low temperatures. The resonance scattering in such a band hybridization system is highly energy-dependent and can be identified from the anomalous temperature-dependent electrical transport mobility: $\frac{d\mu}{dT} > 0$ at low temperature. Such temperature-dependent mobility behavior also indicates that the anomalous thermoelectric transport is not dominated by acoustic phonons.

S11. **Understanding low temperature resistance behavior:**

In our MoS_2/*h*-BN devices, due to the large Debye temperature of MoS_2 (262K), [S11] both 2D Block-Gruneisen ($\propto T^4$) [S12] and electron-phonon resistance ($\propto T$) need to be included. Thus, the total resistance can be described by the following expression [S13] in Kondo hybridization:

$$R = AT^4 + BT + \frac{R_{k0}}{2}\left(1 - \frac{\ln(T/T_K)}{[\ln(T/T_K)^2 + \pi^2 s(s+1)]^{1/2}}\right) + R_0 \quad (1)$$

where s is the effective impurity spin, T_K is the Kondo temperatures and R_0 is the temperature independent term arising from a residual zero temperature resistance. The overall good fits in Fig. 3d in the main manuscript indicate the strong interaction between conduction electrons and localized sulfur vacancy states embedded in MoS_2.

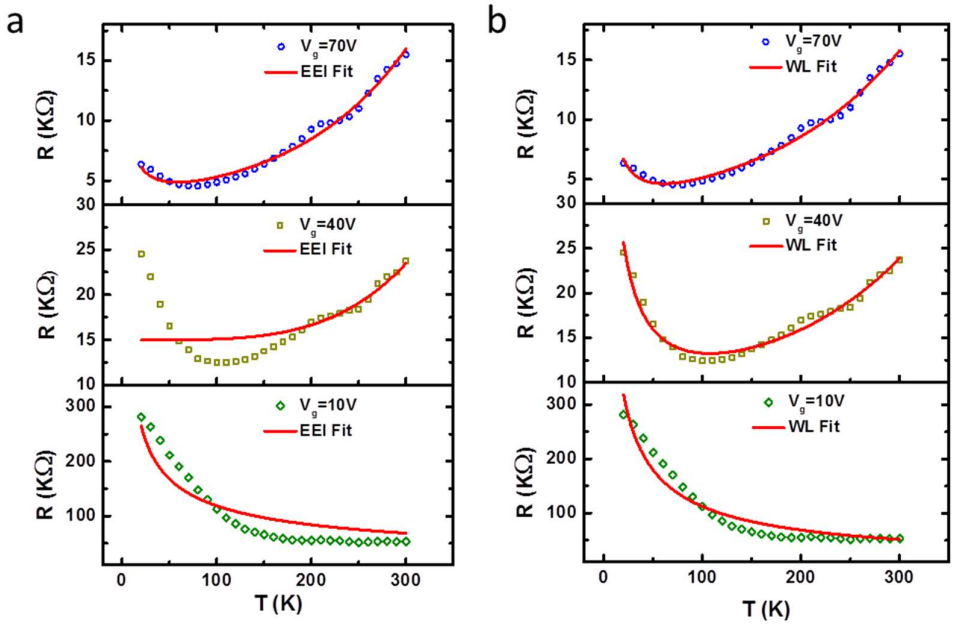

Figure S17: Fitting of electron-electron interactions (EEI) and weak localization (WL) low temperature resistance behavior.

The observation of low-temperature minimum in R(T) may also occur due to strong electron-electron interactions or weak localization from impurities. In the case of electron-electron interactions (EEI), the increasing resistance as T decreases is expected to follow $T^{-1/2}$ dependence [S14] and for weak localization (WL), a $T^{-3/4}$ dependence (weak localization in the dirty limit of dominant electron-electron scattering) is expected [S13,S15,S16]. Here, our resistance data is fitted with the EEI and WL framework: $R = AT^4 + BT + \frac{1}{C+DT^{1/2}}$ (EEI) and $R = AT^4 + BT + \frac{1}{C+DT^{3/4}}$ (WL) as shown in Fig. S17 a&b. The poor curve fittings reveals that the observed resistance minimum in our experiments is neither induced by the EEI nor the WL.

S12. Thermoelectric transport mechanism of MoS_2:

By using single-particle Boltzmann transport equation (BTE) to describe thermoelectric transport in the degenerate region (highly conducting on-state), the BTE reduces to the Mott formula as below [S17]:

$$S_{BTE} = -\frac{\pi^2}{3}\frac{k_B^2 T}{|e|}\left[\frac{\partial \ln \tau}{\partial E} + \left(\frac{\partial \ln g}{\partial E} + \frac{\partial \ln v^2}{\partial E}\right)\right]\Bigg|_{E=E_F} = S_\tau + S_N \quad (2)$$

For MoS_2/SiO_2 device, transport is dominated by acoustic phonon scattering, where τ is energy independent. Hence, the measured Seebeck coefficient of our MoS_2/SiO_2 device can be written as: $S_{total} = S_N + S_{ph}$. In MoS_2/h-BN device, τ is energy-dependent due to the strong resonance scattering. The measured Seebeck coefficient is then given as: $S_{total} = S_N + S_\tau + S_{ph}$ by adding the resonance-scattering term, S_τ.

1. Calculation of diffusive contribution of Seebeck coefficient. S_N is calculated by solving the linearized Boltzmann Transport Equations (BTE) by assuming a single-band material with a parabolic band structure, together with the constant relaxation time approximation. The steady-state solution to the linearized BTE for the diffusive contribution of Seebeck coefficient (S_N) for a 2-Dimensional (2D) material is given as: [S18, S19]

$$S_N = \pm\frac{k_B}{e}\left[\eta - \frac{(r+2)F_{r+1}(\eta)}{(r+1)F_r(\eta)}\right] \quad (3)$$

$$\eta = (E_F - E_C)/k_B T \quad (4)$$

$$F_m(\eta) = \int_0^\infty [x^m/\exp(x-\eta)+1]\,dx \quad (5)$$

where k_B, e, η, r, E_F, E_C, and T represent the Boltzmann constant, charge of an

electron, reduced Fermi potential, scattering parameter, Fermi energy, conduction band minimum energy, and temperature. $F_m(\eta)$ is the m-th order Fermi integral which can be numerically evaluated through numerical integration[S20]. For the calculation of S_N from Eq. (3), the value of scattering parameter (r) used depends on the type of scattering under consideration (Table I), [S18, S21] and the fermi levels $(E_F - E_C)$ for η are calculate from $k_B T ln(exp^{n_{2D}/N_{C,2D}} - 1)$, where $N_{C,2D} = D_{2D} \times k_B T$ is the 2D effective density of states. [S18]

Table I: Scattering parameters of 2-Dimensional materials.

Scattering Mechanism	r
Charged Impurity Scattering	$3/2$
Acoustic Phonon Scattering	0
Intervalley Scattering	0
Strongly screened Coulomb Scattering	$-1/2$

2. Estimation of Seebeck coefficient from phonon-drag effect (S_{ph}): A first-order quantitative estimate[S22,S23] from the theory of phonon-drag in semiconductors is given by $S_{ph} = \beta v_s l_s / \mu T$, which is proposed by Herring [S24]; where v_s is the velocity of sound and l_s is the phonon mean free path. $\beta \subset (0, 1)$ indicates the relative contribution of electron-phonon interaction to electron mobility. β = 1 when the electrons are only scattered by phonons. However, for other scattering processes such as ionized impurity scattering, β = 0. We estimate the temperature-dependent average phonon mean free path using the Debye equation $\kappa = \frac{1}{3} c v_s l_s$, with $v_s = 7900\ m/s$ [S25] and reported values of thermal conductivity [S26, S27], yielding $l_s \sim 5\ nm\ to\ 14\ nm$ for temperatures ranging from 20-300 K as shown in Fig. S 18a. The peak position of l_s is comparable with the phonon-drag peak in Seebeck coefficient as we observed in MoS_2/SiO_2 sample as in Fig. S18b. It is worth to note that the peak position is distinct from the positive peaks in the MoS_2/h-BN sample, as the peak position here does not change with different gate voltages.

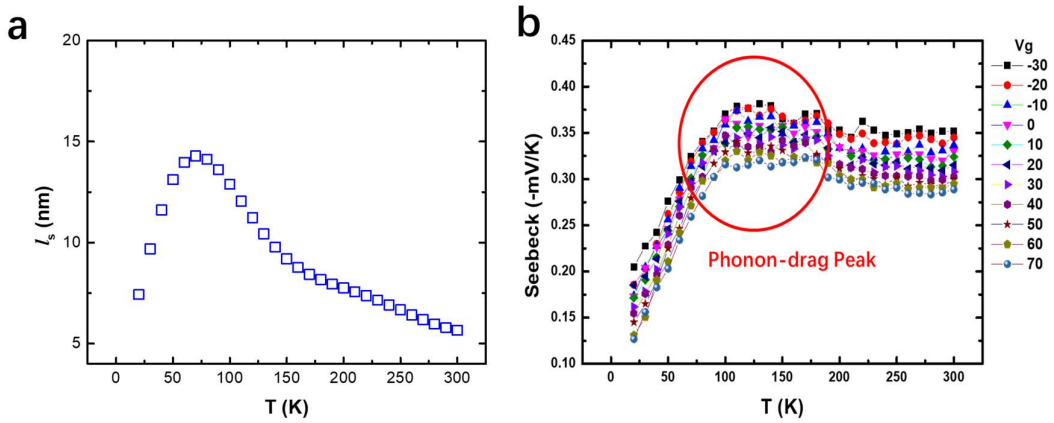

Figure S18: (a) Average phonon mean free path as function of temperature. (b) Seebeck coefficient as function of temperature for different gate voltages of MoS_2/SiO_2 sample.

This estimation is consistent with literature. For temperatures of interest, the thermal conductivity of MoS_2 is dominated by longitudinal acoustic (LA) mode with phonon mean free path ranging from 2 nm to 18 nm for different frequencies [S28]. We remark that this estimated l_s is an effective lower bound involving all phonons, whereas for phonon drag, only phonons with small wave vectors and larger mean free paths are relevant[S24]. Using our measured mobility and assuming $\beta = 1$, the resulting S_{ph} values is estimated in Fig. S19. As can be seen, the S_{ph}~$10^2 \mu V/K$ is comparable to our experiment results shown in Fig. 4C of main manuscript. However, at lower temperatures, the β diverges from unity which explains the peak values of S_{ph} in Fig. 4C. It is worth to note that the magnitude of S_{ph} is not as high as in some low-doping semiconductors because our MoS_2 possesses an equivalent high bulk carrier concentration of ~4.7×10^{18} cm^{-3} with a much higher mobility.

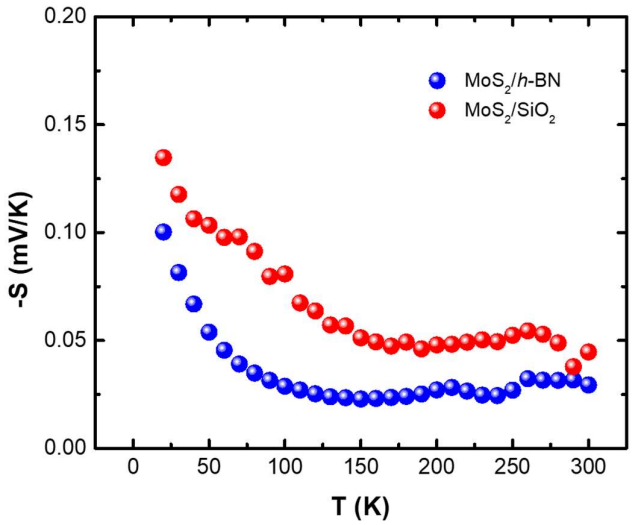

Figure S19: Calculated phonon drag contribution in Seebeck coefficient.

3. Thermoelectric transport in hybridized band: The effect of two band resonance scattering on thermoelectric transport has also been studied in heavy fermions and Kondo-lattice systems where the conduction band electrons have strong interactions with the localized 4f electrons, also called the Abrikosov-Suhl (AS) resonance.[S29] In compounds with cerium (Ce),[S30] which introduces magnetic moments, Seebeck coefficient was found to show a sign-change due to Kondo effects at certain concentrations of Ce, with temperature-dependent trends similar to our results. Here, the Seebeck coefficient can be properly described in the two band approach originating from the Hirst model. [S31,32] In this model, the conduction electrons are scattered by a magnetic impurity band of a Lorentzian form with a width Γ_0 located at ε_0 with respect to the Fermi level. ε_0 can be positive or negative depending on whether the position of the impurity is above or below the Fermi level, respectively. Γ_0 varies with temperature as $\Gamma_0 = T_\Gamma \exp(-T_\Gamma/T)$. T_Γ is a temperature-dependent parameter and represents the quasi-elastic line-width of the Kondo resonance. The final expression for the Seebeck coefficient of resonance scattering can be written as: [S32]

$$S_\tau = A\frac{T\varepsilon_0}{\varepsilon_0^2+[T_\Gamma exp(-T_\Gamma/T)]^2} \quad (6)$$

By eliminating the diffusive (S_N) and phonon-drag (S_{ph}) components from the measured Seebeck coefficient, the resonance-scattered Seebeck coefficient $S_\tau = S_{total} - S_N - S_{ph}$ can be determined. Since the Fermi level of 2D MoS_2 varies with the back-gate and temperature, the relative location ε_0 between the impurity band and Fermi level also changes accordingly. We use equation (6) to fit for fixed carrier concentrations (n= 2×10^{12} cm^{-2}, 1.5×10^{12} cm^{-2} and 0.5×10^{12} cm^{-2}). Fig. S18 a, b and c

show that the temperature-dependent trend in the measured Seebeck coefficient are captured well by this resonance scattering model.

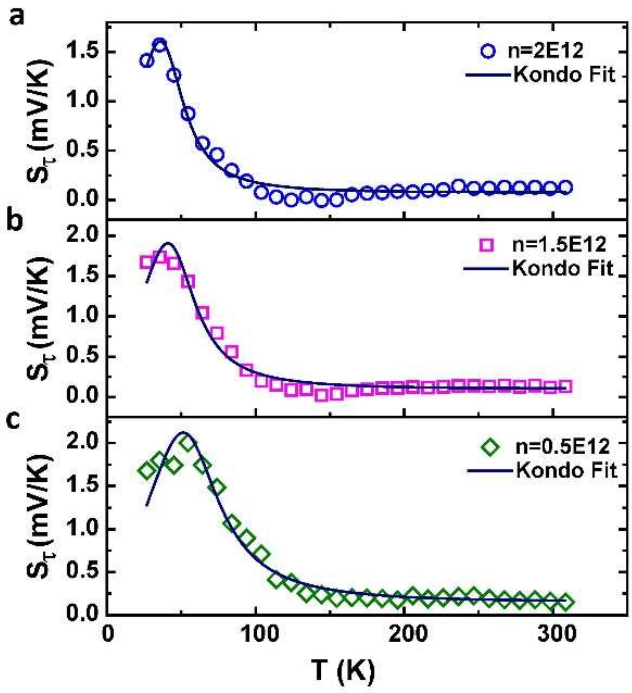

Figure S20: Resonance scattering induced Seebeck coefficient S_τ as a function of temperature at carrier concentration n= 2×10^{12} cm^{-2}, 1.5×10^{12} cm^{-2} and 0.5×10^{12} cm^{-2}. The solid lines are given by the fitting from Eq. (6).

As the temperature decreases from 100K (where the Kondo effect starts to dominate) to 20K, the location of Fermi level shifts from -20 meV to -1 meV. For a Kondo temperature given by k_BT_K ~ 4meV at these doping levels with an impurity state bandwidth of ~15meV, this allows us to obtain the resonance scattering originating from the impurity level and show that it is located between E_c and E_F resulting in a positive Seebeck. The extra state induced by the AS resonance greatly enhances S at low temperatures and explains the appearance of a positive S. Coupled with the –ln(T) upturn of the electrical resistivity at $T < T_K$, the temperature and gate-dependent

behavior of Seebeck coefficient in MoS_2/*h*-BN can now also be explained by adding the contribution from the Kondo scattering.

S13. Additional Seebeck coefficient results:

The absolute $|S|$ decreases with increasing V_g as expected, with an increasing carrier concentration in the MoS_2 channel, which is also consistent with the Mott formula. (Fig. S21)

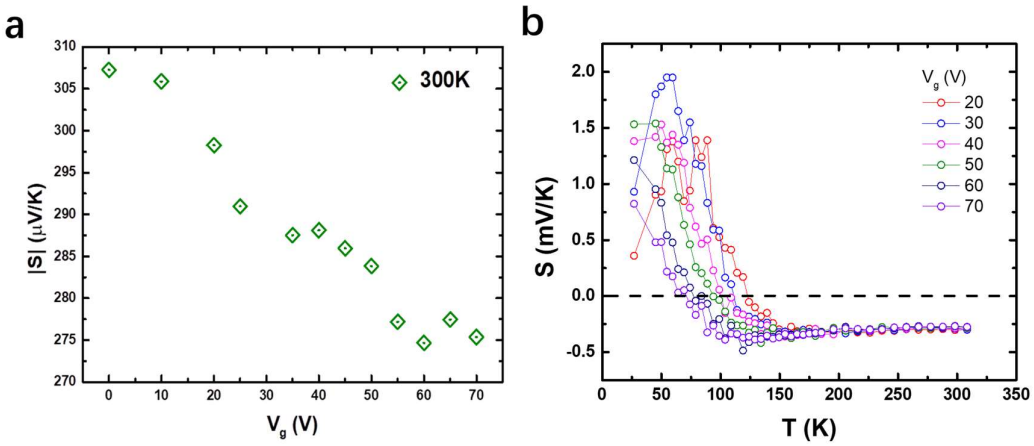

Figure S21: (a) Absolute value of Seebeck coefficient as function of gate voltage at 300K. (b) Seebeck coefficient as function of temperature of MoS_2/*h*-BN sample for different gate voltages.

We also compared the Seebeck coefficient results of our measured MoS_2/*h*-BN devices under different thermal annealing temperatures. MoS_2/*h*-BN_01 and MoS_2/*h*-BN_02 are annealed under 200 °C and 180 °C respectively. From Fig. S22, we can find that both exhibit the same sign-change behavior. However, sample MoS_2/*h*-BN_01 gives a higher Seebeck coefficient at the same gate voltage and the sign-change temperature is also different. This is in agreement with our STM data because annealing at higher

temperatures introduces more sulfur vacancies.

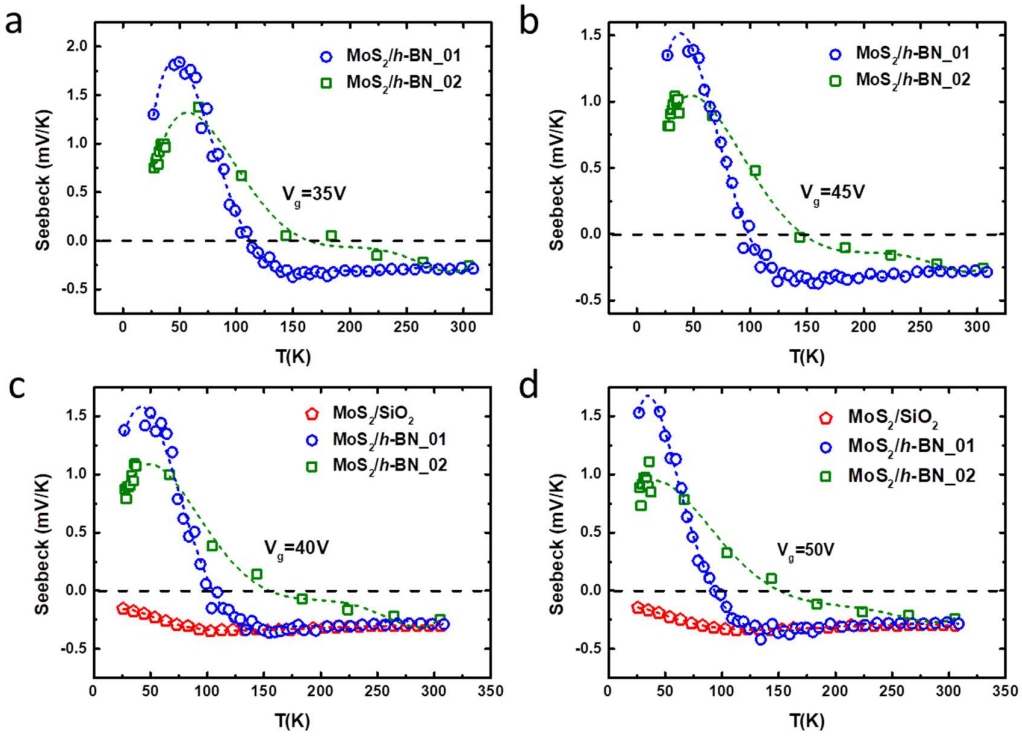

Figure S22: Comparison of the Seebeck coefficient between MoS_2/*h*-BN and MoS_2/SiO_2 samples.

This behavior is also revealed in the comparison of colour contour plot of the *S* values versus back gate voltage V_g and temperature *T* (Fig. S23) for different samples under different anealing temperatures (180 °C, 200 °C and 250 °C). The black dotted line indicates where *S* changes sign from negative to positive values, and the anomalous maximum positive Seebeck is indicated by the intensity of red color on the plot. When we increase the annealing temperature, MoS_2 becomes more n-doped (the threshold voltage shifts to more negative values) and the Fermi level moves towards the conduction band. As seen in Fig. S23, the Kondo temperature decreases as the sample becomes more metallic. Also, the peak value of the Seebeck coefficient seen in the following figure is located at or near the Kondo temperature T_K and hence the Seebeck

maximum and sign change temperature shift towards lower temperatures.

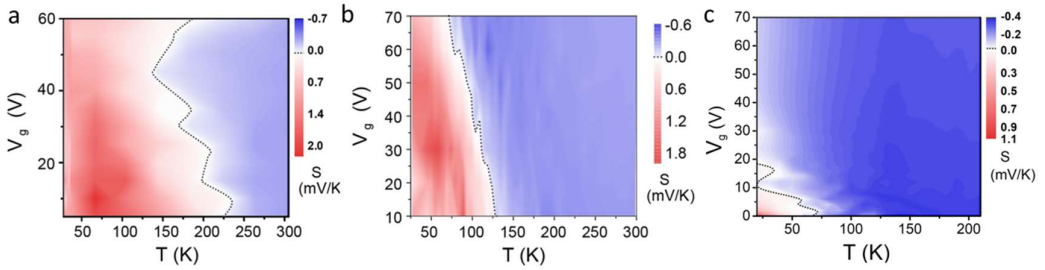

Figure S23: Colour contour plot of the *S* values versus back gate voltage V_g and temperature *T* for different devices annealing at 180 °C (a), 200 °C (b) and 250 °C (c).

In a Kondo system, thermoelectric transport is dominated by strong correlations between the conduction electrons and the magnetic moments of the localized d- or f-electrons at low temperatures [S33]. The spin-flip resonance between the magnetic impurity and the band electrons has been shown to induce a sign change in the Seebeck coefficient [S34], which has been considered as a signature of the Kondo effect in thermoelectric transport [S35]. In fact, these observations confirm that the Seebeck coefficient exhibits a peak at or near the Kondo temperature T_K [S36], which is exactly what we observed in Fig. S23, and further verifies that this sign-change is due to a similar mechanism.

S14. Discussion about the Sign change in Seebeck coefficient:

In general, the Seebeck coefficient is given as the sum of two independent contributions as we discussed in the main manuscript: $S=S_N+S_\tau+S_{ph}$. S_N is the conventional charge carrier diffusion component and S_τ is the scattering component. The sign of S_N is only dependent on the charge carrier type. For example, the sign change in the Seebeck

coefficient is observed in ambipolar systems such as graphene and black phosphorus or in some semimetal like bismuth, where electrons and holes contribute simultaneously to transport. This also happens in charge density wave systems where the opening of a narrow band gap due to the resizing of the Brillouin zone induced by lattice distortion. Table 2 summarizes the sign change in the Seebeck coefficient.

Table 2: Comparison of previous reported change of sign in Seebeck coefficient

Sign change in Seebeck Coefficient	**Materials**	**Reference**
Sign change (**both positive and negative *S* observed**) for electrons-dominant region	MoS_2/*h*-BN	Our work(single material due to defects)
Ambipolar materials: 1. Positive Seebeck for holes-dominant 2. Negative Seebeck for electrons-dominant **3. Sign changes only charge carrier type varies**	Graphene	*Proc. Natl. Acad. Sci*. **113**, 14272-14276 (2016).
	Graphene	*Phys. Rev. Lett.* **102**, 096807 (2009)
	Carbon Nanotubes	*Phys. Rev. Lett.* **91**, 256801 (2003)
	WSe_2	*Nano Lett*. **16**, 2061-2065 (2016)
	Black phosphorus	*Nano Lett.* **16,** 4819-4824 (2016)
1. Positive *S* in some metals when holes filled in the first Brillouin zone. 2. No sign change at hole/electron-dominant region. 3. Semimetal like bismuth, where electrons and holes contribute simultaneously to the transport properties. 4. **Sign changes occurs only when charge carrier type varies**	Copper	*Phys. Rev*. **129**, 138 (1963)
	Copper	*J. Phys. Soc. Jpn*. **25**, 141-150 (1968)
	Bismuth	*J. Phys. C: Solid State Phys. 10 L397(1977)*
1. Sign change due to strong band hybridization and opens secondary narrow band gap in the conduction band. 2. **Band hybridization**	$FeSb_2$	*EPL, 80, 17008 (2007)*
	FeSi	*Phys. Rev. B, 50, 8207(1994)*
1. Band gap opening in the CDW system also allows both electrons and holes to contribute to the thermoelectric transport. 2. **Band hybridization**	$NbSe_3$	*Nano Lett., 19, 415−421 (2019)*
	$TaSe_3$	*Phys. Rev. B, 35, 2687 (1987)*

Remarks: The previously reported sign change in Seebeck coefficient.

S15. Substrate effect and layer thickness dependent thermoelectric transport in MoS_2/h-BN samples:

It is well known that the charge transport properties of 2D materials are extremely sensitive to the underlying substrates. Especially on SiO_2, which is the most widely used substrate for 2D material studies, the scattering of charges is dominated by extrinsic effects such as charged surface states, dangling bonds, impurities substrate surface roughness and remote optical phonons which can mask intrinsic transport properties [S10,S30]. This is especially important at lower temperatures where the phonons are suppressed, and impurity scattering becomes the dominate mechanism controlling charge transport.

On the other hand, *h*-BN is an appealing substrate due to its atomically smooth surface, which can provide an extremely clean surface. Moreover, *h*-BN is known to be relatively free of dangling bonds and charge traps [S37]. It has been proved that by replacing the SiO_2 substrate with *h*-BN, extrinsic scattering effects on 2D materials can be significantly suppressed. The use of *h*-BN substrates has enabled devices with ultralow extrinsic disorder that allow access to intrinsic physics of many 2D materials, for example the integer and fractional quantum Hall effects in graphene [S38], and the hydrodynamic electronic transport in graphene [S39]which can only be observed in graphene/*h*-BN devices [S40]. Such an intrinsic correlated scattering process in graphene

is similar to our study on correlated Kondo resonance scattering in MoS_2/*h*-BN devices. To further elaborate, statistical studies on using *h*-BN as substrate and the effect of layer numbers have been reported by many groups [S37]. It is found that not only does the *h*-BN suppress the effect of extrinsic interfacial scattering, increasing the *h*-BN layer thickness can also reduce such extrinsic interfacial effects to access the intrinsic property of MoS_2. For example, the highest mobility is reported in 6-layer MoS_2 samples [S37]. Another study employing quantum Hall measurements shows a clear 2D quantum confinement effect exhibiting at a small onset magnetic field (1T) of Shubnikov-de Haas oscillations in 6-layer MoS_2. However, for single layer and 4-layer MoS_2, this onset magnetic field increases to around 10T and 5T. This corroborates with what our observations as well: 6-layer MoS_2 offers a better platform for the study of intrinsic transport properties compared to thinner layers.

The effect resulting from the intrinsic sulfur vacancies within the MoS_2 crystal will also become more appreciable in thicker MoS_2, also confirmed by our STM data (Fig. S24) which shows that sulfur vacancies are not only located on the top layer of MoS_2. Similar results have also been reported by many other groups [S41].

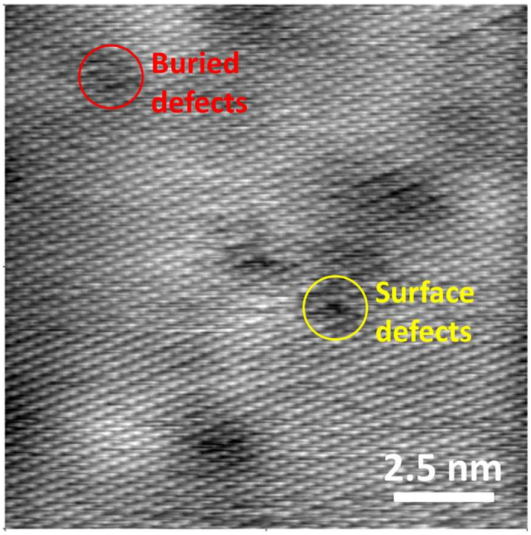

Figure S24: STM topographic images for sulfur vacancies on the surface and under layer.

In fact, the reason why we did not perform an extensive statistical analysis to ascertain exactly how one can correlate the change in magnitude of sub-band splitting and/or S_τ to sulfur vacancy density is precisely because these sulfur vacancies are located both on the surface and within the crystal. The STM does not tell us which layer the sulfur vacancy belongs to, except for the top and second layer. Indeed, in a pristine monolayer sample, this coupling between the sulfur vacancy density and the TE properties would be intriguing. However, in practice, the screening of charges due to the underneath oxide layer prevents such effects due to intrinsic defects manifesting in thermoelectric transport.

As a matter of fact, we attempted to perform additional experiments on single and bilayer samples. For single layer and bilayer MoS_2 devices(Fig. S25), we did not observe any sign change in Seebeck coefficient. The data are reproduced below where they only show negative Seebeck for n-MoS_2 as expected. From our knowledge, the phonon-drag effect induced by the substrate from the leaking phonons is particularly

effective in thinner films. As the film thickness increases, a smaller fraction of the film volume would be accessible to the leaking phonons before they are scattered and the strength of such phonon-drag effect should be weaken [S42]. However, in our case, we did not observe the same trend. Specifically, in our thinnest single-layer MoS_2/*h*-BN sample, no signature of such phonon-drag effect in our temperature-dependent Seebeck coefficient is observed. Besides, the Seebeck coefficient peak in our bilayer MoS_2 device is located around 120K, which is also attributed to the phonon-drag effect in MoS_2 as discussed in the main manuscript. Such observation further clarifies that the sign change in Seebeck coefficient is not originating from the long mean free path phonons in *h*-BN.

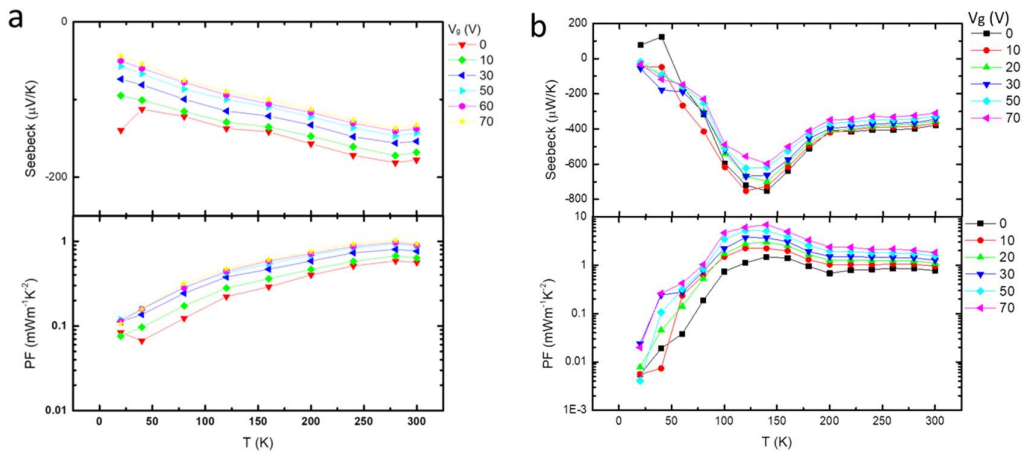

Figure S25: Seebeck coefficient and power factor for single layer (**a**) and bilayer (**b**) MoS_2 on h-BN sample for different temperatures.

References:

S1. Mishchenko, A. *et al.* Twist-controlled resonant tunnelling in graphene / boron nitride / graphene heterostructures. *Nat. Nanotechnol.* **9**, 808–813 (2014).

S2. Bing, D. *et al.* Optical contrast for identifying the thickness of two-dimensional materials. *Opt. Commun.* **406**, 128–138 (2018).

S3. Kresse, G. & Furthmüller, J. Efficient iterative schemes for ab initio total-energy calculations using a plane-wave basis set. *Phys. Rev. B* **54**, 169–186 (1996).

S4. Cui, X. *et al.* Lowerature Ohmic Contact to Monolayer MoS2 by van der Waals Bonded Co/h-BN Electrodes. *Nano Lett.* **17**, 4781–4786 (2017).

S5. Ugeda, M. M. *et al.* Giant bandgap renormalization and excitonic effects in a monolayer transition metal dichalcogenide semiconductor. *Nat. Mater.* **13**, 1091–1095 (2014).

S6. Baugher, B. W. H., Churchill, H. O. H., Yang, Y. & Jarillo-Herrero, P. Intrinsic electronic transport properties of high-quality monolayer and bilayer MoS2. *Nano Lett.* **13**, 4212–4216 (2013).

S7. Cui, X. *et al.* Multi-terminal transport measurements of MoS2 using a van der Waals heterostructure device platform. *Nat. Nanotechnol.* **10**, 534–540 (2015).

S8. Kaasbjerg, K., Thygesen, K. S. & Jacobsen, K. W. Phonon-limited mobility in n-type single-layer MoS2 from first principles. *Phys. Rev. B* **85**, 115317 (2012).

S9. Fivaz, R. & Mooser, E. Mobility of charge carriers in semiconducting layer structures. *Phys. Rev.* **163**, 743–755 (1967).

S10. Radisavljevic, B. & Kis, A. Mobility engineering and a metal-insulator transition in monolayer MoS2. *Nat. Mater.* **12**, 815–820 (2013).

S11. Peng, B. *et al.* Thermal conductivity of monolayer MoS2, MoSe2, and WS2: Interplay of mass effect, interatomic bonding and anharmonicity. *RSC Adv.* **6**, 5767–5773 (2016).

S12. Efetov, D. K. & Kim, P. Controlling electron-phonon interactions in graphene at ultrahigh carrier densities. *Phys. Rev. Lett.* **105**, 256805 (2010).

S13. Barua, S., Hatnean, M. C., Lees, M. R. & Balakrishnan, G. Signatures of the Kondo effect in VSe2. *Sci. REPORTS* | **7**, 1–10 (2017).

S14. Maritato, L. *et al.* Low-temperature resistivity of La0.7Sr0.3MnO3 ultra thin films: Role of quantum interference effects. *Phys. Rev. B* **73**, 094456 (2006).

S15. Kaveh, M. & Mott, N. F. Universal dependences of the conductivity of metallic disordered systems on temperature, magnetic field and frequency. *J. Phys. C Solid State Phys.* **15**, (1982).

S16. Lee, P. A. & Ramakrishnan, T. V. Disordered electronic systems. *Rev. Mod. Phys.* **57**, 287–337 (1985).

S17. Cutler, M. & Mott, N. F. Observation of anderson localization in an electron gas. *Phys. Rev.* **181**, 1336–1340 (1969).

S18. Ng, H. K., Chi, D. & Hippalgaonkar, K. Effect of dimensionality on thermoelectric powerfactor of molybdenum disulfide. *J. Appl. Phys.* **121**, 204303 (2017).

S19. Pichanusakorn, P. & Bandaru, P. R. The optimal Seebeck coefficient for obtaining the maximum power factor in thermoelectrics. *Appl. Phys. Lett.* **94**, 1–4 (2009).

S20. Mohankumar, N. & Natarajan, A. The accurate numerical evaluation of half-order Fermi-Dirac Integrals. *Phys. Status Solidi* **188**, 635–644 (1995).

S21. Lundstrom, M. Fundamentals of Carrier Transport , 2 nd Edition. (2004).

S22. Takahashi, H., Okazaki, R., Yasui, Y. & Terasaki, I. Low-temperature magnetotransport of the narrow-gap semiconductor FeSb2. *Phys. Rev. B* **84**, 205215 (2011).

S23. Sales, B. C. *et al.* Transport , thermal , and magnetic properties of the narrow-gap semiconductor CrSb2. *Phys. Rev. B* **86**, 235136 (2012).

S24. Herring, C. Theory of the Thermoelectric Power of Semiconductors. *Phys. Rev.* **96**, 1163–1187 (1954).

S25. Zhang, W., Huang, Z., Zhang, W. & Li, Y. Two dimensional semiconductors with possible high room temperature mobility. *Nano Res.* (2014). doi:10.1007/s12274-014-0532-x

S26. Aiyiti, A. *et al.* Thermal conductivity of suspended few-layer MoS2. *Nanoscale* **10**, 2727–2734 (2018).

S27. Yarali, M. *et al.* Effects of Defects on the Temperature-Dependent Thermal Conductivity of Suspended Monolayer Molybdenum Disulfide Grown by Chemical Vapor Deposition. *Adv. Funct. Mater.* **27**, 1704357 (2017).

S28. Cai, Y., Lan, J., Zhang, G. & Zhang, Y. Lattice vibrational modes and phonon thermal conductivity of monolayer MoS2. *Phys. Rev. B* **89**, 035438 (2014).

S29. Grewe, N. & Steglich, F. Chapter 97 Heavy fermions. in *Handbook on the Physics and Chemistry of Rare Earths: Chapter 97 Heavy fermions* **14**, 343–474 (1991).

S30. Gottwick, U., Gloos, K., Horn, S., Steglich, F. & GREWE, N. Transport coefficients of intermediate valent CeNiX intermetallic compounds. *J. Magn. Magn. Mater.* **47&48**, 536–538 (1985).

S31. Hirst, L. L. Electronic properties of 4f substances at configuration crossover. *Phys. Rev. B* **15**, 1–9 (1977).

S32. Kaczorowski, D. & Gofryk, K. Thermoelectric power of Ce-based intermediate valent systems. *Solid State Commun.* **138**, 337–340 (2006).

S33. Sparn, G., Lieke, W., Gottwick, U. & Grewe, N. Low-Temperature Transport Properties F . Steglich. *J.Mag.Mag.Mat.* **47&48**, 521–523 (1985).

S34. Bhattacharjee, A. K. & B. Coqblin. Thermoelectric power of compounds with cerium: Influence of the crystalline field on the Kondo effect. *Phys. Rev. B* **13**, 3441–3451 (1976).

S35. Gratz, E. *et al.* CeCu 2 : a new Kondo lattice showing magnetic order. *J. Phys. F Met. Phys.* **15**, 1975–1986 (1985).

S36. Franz, W., Griebel, A., Steglich, F. & Wohlleben, D. Transport Properties of LaCu2Si2 and CeCu2Si2 Between 1.5 K and 300 K * * *. *Z. Phys. B* **31**, 7–17 (1978).

S37. Dean, C. R. *et al.* Boron nitride substrates for high-quality graphene electronics. *Nat. Nanotechnol.* **5**, 722–726 (2010).

S38. Dean, C. R. *et al.* Multicomponent fractional quantum Hall effect in graphene.

Nat. Phys. **7**, 693–696 (2011).

S39. Crossno, J. *et al.* Observation of the Dirac fluid and the breakdown of the Wiedemann-Franz law in graphene. *Science (80-.).* **351**, 1058–1061 (2016).

S40. Ghahari, F. *et al.* Enhanced Thermoelectric Power in Graphene : Violation of the Mott Relation by Inelastic Scattering. *Phys. Rev. Lett.* **116**, 136802 (2016).

S41. Lu, C., Li, G., Mao, J., Wang, L. & Andrei, E. Y. Bandgap, Mid-Gap States, and Gating Effects in MoS2. *Nano Lett.* **14**, 4628–4633 (2014).

S42. Wang, G., Endicott, L., Chi, H., Lošt'Ák, P. & Uher, C. Tuning the temperature domain of phonon drag in thin films by the choice of substrate. *Phys. Rev. Lett.* **111**, 1–5 (2013).